Marine ice sheet dynamics: Hysteresis and neutral equilibrium

Gaël Durand, Olivier Gagliardini, B. de Fleurian, T. Zwinger, Emmanuel Le Meur

Marine ice sheet dynamics: Hysteresis and neutral equilibrium

G. Durand,[1] O. Gagliardini,[1] B. de Fleurian,[1] T. Zwinger,[2] and E. Le Meur[1]

Received 3 October 2008; revised 5 May 2009; accepted 13 May 2009; published 5 August 2009.

[1] The stability of marine ice sheets and outlet glaciers is mostly controlled by the dynamics of their grounding line, i.e., where the bottom contact of the ice changes from bedrock or till to ocean water. The last report of the Intergovernmental Panel on Climate Change has clearly underlined the poor ability of models to capture the dynamics of outlet glaciers. Here we present computations of grounding line dynamics on the basis of numerical solutions of the full Stokes equations for ice velocity, coupled with the evolution of the air ice– and sea ice–free interfaces. The grounding line position is determined by solving the contact problem between the ice and a rigid bedrock using the finite element code Elmer. Results of the simulations show that marine ice sheets are unstable on upsloping beds and undergo hysteresis under perturbation of ice viscosity, confirming conclusions from boundary layer theory. The present approach also indicates that a 2-D unconfined marine ice sheet sliding over a downsloping bedrock does not exhibit neutral equilibrium. It is shown that mesh resolution around the grounding line is a crucial issue. A very fine grid size (<100 m spacing) is needed in order to achieve consistent results.

Citation: Durand, G., O. Gagliardini, B. de Fleurian, T. Zwinger, and E. Le Meur (2009), Marine ice sheet dynamics: Hysteresis and neutral equilibrium, *J. Geophys. Res.*, *114*, F03009, doi:10.1029/2008JF001170.

1. Introduction

[2] Marine ice sheets, i.e., ice sheets grounded on bedrock below sea level, can play a key role in the climatic system. Their eustatic contribution to sea level rise can be explained by a decrease of the surface mass balance inland, an increase of the ice discharge into ocean through outlet glaciers and a retreat of the grounding line [*Alley et al.*, 2005]. The estimated sea level rises by 2100 detailed in the fourth assessment of *Intergovernmental Panel on Climate Change* [2007] include a constant (through time) contribution rate attributed to dynamical effects. However IPCC acknowledges the limited understanding of the relevant processes and consequently a poor reliability of model prediction. The poor ability to understand and model the processes at the root of the currently observed dynamical effects may arise from their small spatial scales compared with the entire ice sheet. Particularly, understanding the dynamics of the grounding line to different perturbations seems to be a key issue and this paper aims at contributing to this aspect.

[3] Grounded ice sheet flow is dominated by horizontal shearing while the ice shelf flow is dominated by longitudinal stretching and lateral shearing. The two types of flow are coupled across a transition zone (ice stream) near the grounding line where longitudinal and shear stresses are of the same order of magnitude. Ice sheet models are usually vertically integrated and use different sets of approximated equations to compute ice deformation within these two regions [*Huybrechts and de Wolde*, 1999; *Ritz et al.*, 2001]. Coupling between the two flow regimes is then awkward as none of the approximated equations is suitable in the transition zone. This leads to strong approximations in the coupling between the two flow regimes. Efforts to compare different models were initiated during the EISMINT project [*Huybrechts et al.*, 1996], and revealed no consensus on the issue of grounding line dynamics [*Huybrechts*, 1997]. More recently, *Vieli and Payne* [2005] have shown the poor ability of marine ice sheet models to give consistent prognostic results and have concluded that no state-of-the-art model was able to predict grounding line migration.

[4] A long debate on the dynamics of such ice sheets was initiated in the seventies when *Weertman* [1974] proposed that a marine ice sheet which lies on an upward sloping bed is unstable. *Weertman* [1974] asserted that ice discharge through the vertical section located at the grounding line should increase with ice thickness. As a consequence of a slight retreat in grounding line position, ice thickness there would increase and then enhance ice discharge through the vertical gate at the grounding line. A positive feedback is initiated as the increase of ice discharge should lead to a further thinning of the ice sheet and thus, a further retreat of the grounding line. This raises some questions about the stability of the West Antarctic ice sheet for which the bed close to its central part is generally deeper than at the grounding line. More particularly, Pine Island Glacier together with its Amundsen Coast neighbor Thwaites Glacier drains a large part of the West Antarctic ice sheet (40% in volume); they exhibit a bedrock topography which

[1] Laboratoire de Glaciologie et Géophysique de l'Environnement, UJF-Grenoble, CNRS, Saint-Martin-d'Hères, France.
[2] CSC-IT Center for Science Ltd., Espoo, Finland.

0148-0227/09/2008JF001170

deepens considerably inland and show considerable retreat of their grounding line during the last decade [*Rignot*, 1998; *Rignot et al.*, 2002; *Payne et al.*, 2004].

[5] An abundant literature dealing with the coupling between grounded ice sheet and floating ice shelf, and identifying this transition zone as a crucial control of the marine ice sheet dynamics, was motivated by the initial discussion proposed by Weertman [e.g., *Van der Veen*, 1985; *Hindmarsh*, 1993, 1996; *Chugunov and Wilchinsky*, 1996; *Vieli and Payne*, 2005; *Pattyn et al.*, 2006; *Schoof*, 2007b, 2007a]. The instability hypothesis has been controversial and *Hindmarsh* [1993, 1996] argued that the coupling between the shelf and the grounded part should have a negligible impact on the dynamics of the grounded ice sheet and concluded that a marine ice sheet should be neutrally stable with respect to displacement in grounding line position. Recently, the instability hypothesis has been strongly reinforced, on the basis of a boundary layer (BL) theory by *Schoof* [2007a]. Application of his theory led *Schoof* [2007b] to conclude that (1) no steady grounding line can be found on an upsloping bed; (2) marine ice sheets with overdeepening beds can undergo hysteresis behavior of the grounding line position under perturbation of sea level, accumulation rate, basal slipperiness or ice viscosity and (3) marine ice sheet does not exhibit neutral equilibrium. As a more general conclusion, results from BL theory confirms the proposed assertion of *Weertman* [1974] that grounding line flux is a function of ice thickness at the grounding line in the case of a 2-D flow problem with no lateral shearing in ice shelf.

[6] The main focus of this paper is to test the validity of the instability hypothesis using an ice flow model. The model solves the full Stokes equations and therefore includes all force components acting in the mechanical coupling between ice shelf and grounded ice sheet. A similar approach has been initiated by *Lestringant* [1994] and was used more recently by *Nowicki and Wingham* [2008]. We restrict our study to a flow line simulation over a domain that lies between a dome and a calving front. The ice body is bounded by two free surfaces, the upper interface ice/air and the bottom interface between the ice and the sea. The evolution of the two free interfaces is determined by solving a local transport equation. We assume a rigid and impenetrable bedrock so that the link between the ice and the bedrock is treated as a contact problem: the ice cannot penetrate the bedrock but is allowed to move away from it. Resolution of the contact problem has been inspired from previous studies on subglacial cavities, namely the works done by *Iken* [1981], *Schoof* [2005] and *Gagliardini et al.* [2007]. Those equations have been implemented within the finite element (FE) code Elmer (Elmer manuals, available at http://www.csc.fi/elmer/) and are explained in section 2. Details on the numerics follow in section 3.

[7] In order to investigate the marine ice sheet instability hypothesis, and more particularly to compare our approach to the BL theory, we have followed the modeling framework designed for the Marine Ice sheet Model Intercomparison Project (MISMIP) (C. Schoof et al., 2008; available at http://homepages.ulb.ac.be/~fpattyn/mismip/). Simulations are conducted using an overdeepening bed, and the ice sheet is forced by step changes in fluidity. Main conclusions of BL theory (points detailed above) will be tested in details in section 4.

2. Formulation of the Problem

2.1. Notations and Main Hypothesis

[8] The geometry is restricted to a two-dimensional plane flow perpendicular to the y direction. The flow is along the x direction and the z axis is the vertical upward pointing axis, as illustrated in Figure 1. The left boundary of the domain is assumed to be a symmetry axis and the shelf ends at the right side of the domain. The problem to be solved consists in the gravity-driven flow of isothermal, incompressible and nonlinear viscous ice, sliding over a rigid bedrock $z = b(x)$ assuming a nonlinear friction law for the grounded part and normal stress on the interface in contact with the ocean. The grounding line is defined as the last node in contact with bedrock and will be denoted x_G. The condition imposed by the sea at the bottom part of the ice shelf will be defined below in detail.

[9] The constitutive law for the ice behavior is given by a power law (Glen's flow law in Glaciology):

$$S_{ij} = 2\eta D_{ij}, \tag{1}$$

where $\mathbf{S}$ is the deviatoric stress tensor, $D_{ij} = (u_{i,j} + u_{j,i})/2$ are the components of the strain rate tensor, $\mathbf{u}$ is the velocity vector, and comma denotes differentiation. The effective viscosity η can be expressed as

$$\eta = B^{-1/n}\gamma_e^{(1-n)/n}, \tag{2}$$

where the strain rate invariant γ_e, when larger than $\gamma_{\min} = 1.10^{-15}$, is defined as

$$\gamma_e^2 = 2D_{ij}D_{ij}. \tag{3}$$

We adopt the common assumption $n = 3$ which renders the rheology nonlinear. In equation (2), the fluidity parameter B is a constant since ice is assumed isothermal (see Table 1).

2.2. Governing Equations

[10] The problem to be solved is the flow of an ice body delimited by two free surfaces, namely the upper interface $z = z_s(x, t)$ and the free interface $z = z_b(x, t)$ that separates ice from bed or sea. The length of the latter, starting at the grounding line $x_G(t)$, is not known in advance, and is therefore part of the solution.

[11] The ice flow is determined by solving the Stokes problem, consisting in the mass conservation equation in case of incompressibility:

$$\mathrm{tr}\mathbf{D} = \mathrm{div}\mathbf{u} = 0, \tag{4}$$

and the momentum equations:

$$\mathrm{div}\boldsymbol{\sigma} = \rho_i\mathbf{g}, \tag{5}$$

where $\boldsymbol{\sigma} = \mathbf{S} - p\mathbf{I}$ is the Cauchy stress with $p = -\mathrm{tr}\boldsymbol{\sigma}/3$ the isotropic pressure, ρ_i the ice density and $\mathbf{g}$ the gravity vector.

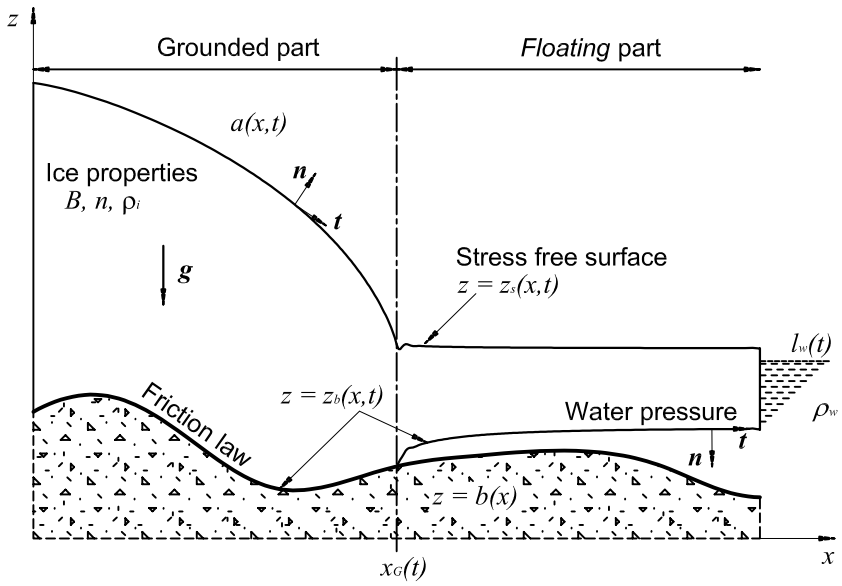

Figure 1. Geometry and nomenclature of the investigated problem.

[12] The evolution of the two free interfaces is determined by solving a local transport equation:

$$\frac{\partial z_j(x,t)}{\partial t} + u_x(x,z_j)\frac{\partial z_j(x,t)}{\partial x} - u_z(x,z_j) = a_j(x,t), \qquad (6)$$

where subscript j denotes the upper interface ($j = s$) or the bottom one ($j = b$), u_i (x, z_j) is the velocity in the horizontal ($i = x$) and vertical ($i = z$) directions for the considered interface and a_j (x, t) is the accumulation/ablation. In what follows, the accumulation on the upper interface a_s is a vertical flux strictly uniform in space and constant in time whereas the bottom melting/accretion is neglected (see Table 1).

[13] Assuming a rigid, impenetrable bedrock $z = b(x)$, the following topological conditions must be fulfilled by z_s and z_b:

$$z_s(x,t) > z_b(x,t) \geq b(x) \quad \forall x,t. \qquad (7)$$

2.3. Boundary Conditions

2.3.1. Upper Interface $z = z_s$ (x, t)

[14] Because the atmospherical pressure is insignificant with regards to the considered stresses, the upper interface is considered as a stress free surface, which implies that $\sigma_{nn}|_s = \mathbf{n}\cdot(\boldsymbol{\sigma}\cdot\mathbf{n})|_s = p_{atm} \approx 0$, and $\sigma_{nt}|_s = \mathbf{t}\cdot(\boldsymbol{\sigma}\cdot\mathbf{n})|_s = 0$ where $\mathbf{n}$ is the unit normal vector of the interface pointing outward and $\mathbf{t}$ is the tangent. Here $|_s$ denotes value taken at the upper free surface. As a consequence of the variational formulation used in Elmer, this stress free condition is inherent (natural boundary condition), such that no explicit condition has to be applied for the Stokes problem.

2.3.2. Dome and Calving Front

[15] The dome is assumed to be a symmetry axis for the flow problem, which implies that u_x (0, z) = 0. The end of the domain, where the shelf cuts off, can be seen as the point where icebergs are calving. In our 2-D problem, with no lateral friction prescribed, the exact position of the calving front is not an issue because it does not influence the upstream flow. This interface is subject to a normal stress due to the water pressure p_w (z, t), which evolves vertically as

$$p_w(z,t) = \begin{cases} \rho_w g(l_w(t) - z), & z < l_w(t) \\ 0, & z \geq l_w(t) \end{cases}, \qquad (8)$$

where ρ_w is the seawater density and l_w the sea level.

2.3.3. Bottom Interface $z = z_b$ (x, t)

[16] At the base, the unilateral link between the ice and the bedrock can be treated as a contact problem; in other words the ice cannot penetrate the bedrock but is allowed to move away from it. For simplicity, it is assumed that there are no cohesive forces to be overcome before the ice can move away from the bed. At a given point x, ice is assumed to be in contact with the bedrock if the ice touches the bed and the normal stress $\sigma_{nn}|_b = \mathbf{n}\cdot(\boldsymbol{\sigma}\cdot\mathbf{n})|_b$ exerted by the ice is larger than the seawater pressure ($|_b$ denotes the value taken at the bottom interface). Conversely, the ice is assumed to be in contact with the sea if the bottom interface lies above the bed, or, if the ice touches the bed but the sea water pressure is larger than the normal stress. This can be summarized as the following: (1) the ice/bedrock boundary condition applies if

$$z_b(x,t) = b(x) \quad \text{and} \quad -\sigma_{nn}|_b > p_w(z_b,t) \qquad (9)$$

Table 1. Values of the Parameters Used in This Study

Parameter	Value	Units
a_s	0.3	m a^{-1}
a_b	0	m a^{-1}
n	3	
C	2.5 × 10^4	Pa m$^{-1/3}$ a$^{1/3}$
m	1/3	
ρ_w	1025	kg m^{-3}
ρ_i	920	kg m^{-3}
g	9.81	m s^{-2}

and (2) the ice/sea boundary condition applies if

$$z_b(x,t) > b(x)\,,$$
$$\text{or } z_b(x,t) = b(x) \text{ and } -\sigma_{nn}|_{\mathrm{b}} \le p_w(z_b,t). \tag{10}$$

The way this contact problem is actually solved is discussed in section 3.

[17] For the flow problem, two different boundary conditions have to be applied, depending on whether the ice is in contact with the bedrock or with the sea. For the ice/bedrock boundary condition, a nonlinear friction law is applied:

$$\tau_b = \mathbf{t}\cdot(\boldsymbol{\sigma}\cdot\mathbf{n})|_{\mathrm{b}} = C|u_b|^{m-1}u_b, \tag{11}$$

where τ_b is the basal shear stress, $u_b = \mathbf{u}\cdot\mathbf{t}|_{\mathrm{b}}$ the sliding velocity at the base and $\mathbf{t}$ the tangent vector to the interface z_b. The two parameters C and m entering the friction law are given in Table 1. Melting orthogonal to the basal bedrock interface is not taken into account, so that $\mathbf{u}\cdot\mathbf{n}|_{\mathrm{b}} = 0$.

[18] For the ice/sea boundary condition, the normal stress is equal to the buoyancy seawater pressure (8) and the tangential friction is null, i.e., $\sigma_{nt}|_{\mathrm{b}} = \mathbf{t}\cdot(\boldsymbol{\sigma}\cdot\mathbf{n})|_{\mathrm{b}} = 0$.

[19] For the bottom free interface, the non penetration condition (7) is enforced using the contact method to solve the imposed variational inequality. This method is presented in detail in section 3. For all points in contact with the bed (as previously defined), the Dirichlet condition $z_b = b$ is imposed when solving (6).

3. Numerical Implementation

[20] We first give some general settings and we then present in more details five specific and technical points of the modeling approach.

3.1. General Settings

[21] The Stokes equations and the free surface equations for the upper and lower interfaces are solved in a coupled manner using an explicit time stepping scheme. The mesh is composed of linear elements and the Stokes equations are stabilized using the residual free bubbles method [*Baiocchi et al.*, 1993]. Because of the hyperbolic nature of equation (6) the standard Galerkin method does not apply. Stabilization is obtained by applying the method as proposed by *Donea and Huerta* [2003, p. 172] and presented in detail by *Gagliardini and Zwinger* [2008].

3.2. Contact Forces

[22] When computing the flow solution at time t_{i+1}, the new position of the grounding line, x_G (t_{i+1}) is unknown. To determine which boundary conditions have to be applied to a node belonging to the bottom interface, conditions (9) and (10) have to be examined. As the stress quantity is not accessible directly from the flow solution (only velocity and isotropic pressure are), the residual of the Stokes system is used instead. The residual is defined as

$$\mathbf{R} = \mathbf{K}\mathbf{U} - \mathbf{F}, \tag{12}$$

where $\mathbf{K}$ is the matrix of the linearized system obtained by applying a fixed point iteration, $\mathbf{U}$ the velocity pressure vector solution and $\mathbf{F}$ representing the body force including contributions from the damping and stabilization (see section 3.4 and equation (15)). For an exact solution of the Stokes system, its residual should be null except for nodes where a Dirichlet boundary condition is applied. In this latter case, the residual is equal to the contact force induced by prescribing a value for this degree of freedom. On the other hand, the water pressure is integrated over the element boundary face according to the shape function, therefore providing the nodal force $\mathbf{F}_w$ exerted by the water. The normal stress in (9) and (10) is then replaced by the corresponding residual contact force $\mathbf{R}$, whereas the water pressure is replaced by the corresponding nodal force $\mathbf{F}_W$. By construction these forces are not local conditions but represent a spatial mean according to the chosen shape function. Using nodal forces rather than stress is highly advantageous: (1) evaluating the residual comes at almost no cost as long as the original stiffness matrix (which has not undergone the setting of Dirichlet conditions) has been stored for later use and (2) there is not a unique way to determine the nodal stress and solution may differ.

3.3. Nonlinearities of the Problem

[23] From section 2, one can see that three nonlinearities have to be solved for the present flow problem: the nonlinear viscous flow relation (equation (2)), a nonlinear friction law (equation (11)), and the solution-dependent position of the grounding line. For a given time step i, all these nonlinearities are treated during the iterations j of the Stokes equations. For the viscous law and the friction law, the effective viscosity (2) and an effective sliding parameter, defined as $C|u_b|^{m-1}$ from the linearization of (11), are evaluated at the iteration j using the velocity field from the previous iteration $j-1$ of the nonlinear loop. The convergence of the nonlinear system is first solved assuming a fixed grounding line at the position calculated at time step $i-1$, until relative change of the Euclidean norm of the solution becomes less than 10^{-3}. Thereafter, conditions (9) and (10) are examined, and the nodes on the bedrock for which the residual force $\mathbf{R}$ falls below the water force F_w are no longer under Dirichlet condition, but subjected to the ice/sea boundary condition. During the following iterations j of the Stokes equations, if a newly released node shows a penetrating velocity, i.e., if $\mathbf{u}\cdot\mathbf{n} > 0$, the Dirichlet condition is reimposed for this node. Convergence of the Stokes system is assumed to be obtained once the relative change of the norm of the solution becomes less than 10^{-5}. However, if the convergence criterium fails after j = 100 iterations, Stokes resolution is stopped and the last estimation is kept. Note that this rather crude procedure only happens with unrealistic geometry, e.g., ice slab imposed as initial condition of the numerical experiment (see section 4.1).

3.4. Buoyancy Stress Condition

[24] The sea exerts a buoyancy pressure as defined in (8) to the bottom interface z_b (x, t). This condition is simply imposed by equating the imposed normal stress to the buoyancy sea pressure:

$$\sigma_{nn}|_{\mathrm{b}}(t) = -\rho_w g(l_w(t) - z_b(x,t)), \tag{13}$$

where z_b (x, t), the vertical position of the lower interface of the ice body at time t, is unknown. Taking the values of z_b (x, t) at $t - \mathrm{d}t$ destabilizes the numerical scheme, because a small hydrostatic disequilibrium induces large vertical velocity, and consequently very large geometrical changes.

[25] To stabilize the problem, a time-dependent scheme for the interface elevation is introduced. From equation (6), the interface elevation at time t is approximated by a Taylor series:

$$z_b(x,t) = z_b(x,t-\mathrm{d}t) + u_n\sqrt{1+(\partial z_b/\partial x)^2}\mathrm{d}t\,, \qquad (14)$$

where $u_n \sqrt{1 + (\partial z_b/\partial x)^2}\ \mathrm{d}t$ represents the contribution of velocity to the vertical displacement of the interface elevation during dt. The sea stress condition (13) is then rewritten as

$$\sigma_{nn}|_{\mathrm{b}}(t) = -\rho_w g(l_w(t) - z_b(x,t-\mathrm{d}t)) + C_n u_n, \qquad (15)$$

where $C_n = \rho_w\, g\sqrt{1 + (\mathrm{d}z_b/\mathrm{d}x)^2}\ dt$ can be seen to operate like a normal friction coefficient. C_n acts like a damper on the bottom interface so that the normal stress induced by $C_n\, u_n$ will counteract the buoyancy stress and avoid a too large displacement that would arise even for a small disequilibrium of the bottom free interface. Because of the negative value of u_n, this term decelerates any movement away from the equilibrium and renders the numerical scheme stable.

3.5. Nonpenetration Condition for the Free Surfaces

[26] The variational formulation of (6) in index notation has the form

$$M_{ij}z_j = f_i.$$

Here z_j and f_i are the jth and ith entry of the solution and the force vector, with the latter containing contributions from the accumulation, a, as well as the numerical stabilization and the vertical velocity. For the lower interface z_b, this linear equation has to be solved with two geometrical constraints given by (7), imposing an upper $z_j \le z_s$ (x, t) and a lower limit $z_j \ge b(x)$. Those are solved by a simple, but effective iterative contact algorithm. In what follows, an inactive node denotes a node which fulfills the geometrical constraints (7) and it is the contrary for an active node.

[27] 1. Inactive nodes with values violating one of the geometrical constraints given in (7) are marked as active. The marker distinguishes between a violation of the upper or the lower geometrical constraint.

[28] 2. A node formerly indicated as active, x_j, for which its solution z_j fell back within the constraints is released from the list of active nodes only if the residual r_j shows the correct sign. In the case of a former exceeded upper limit, this criterion is $r_j > 0$. If in earlier iteration steps the free interface fell bellow the lower limit, the opposite sign, i.e., $r_j < 0$, is necessary to drop x_j from the list.

[29] 3. If an element node x_j is marked active, its contribution to the system matrix is manipulated such that

$$M_{ij} \to M'_{ij} = \delta_{ij}.$$

Here δ_{ij} is the Kronecker symbol. Depending on whether an upper limit has been exceeded or $z(x_j)$ fell below the lower limit, the force vector is manipulated such that either $f_i \to f'_i = z_s\ (x_j)$ or $f'_i = b(x_j)$. Technically, this is equivalent to a Dirichlet condition for the nodal entry z_j to either $z_j = z_s\ (x_j)$ (upper limit) or $z_j = z_s\ (x_j)$ (lower limit).

[30] 4. The system with the manipulated matrix and force vector is solved, leading to the solution z_i.

[31] 5. The residual of the not manipulated equation system with respect to this solution is given by

$$r_i = M'_{ij}z_j - f'_i.$$

The residual can be interpreted as the necessary volume added to (in case of lower limit) or removed from (in case of upper limit) the node per unit time needed to comply with (7).

[32] The whole procedure given above is repeated until the relative change of the norm $(z_i\, z_i)^{1/2}$ falls under the given threshold 10^{-6}, indicating convergence of the solution. This method, besides having the advantage of being consistent, showed increased numerical stability as well as enhanced convergence in comparison to a penalty formulation or the earlier applied Uzawa algorithm [*Gagliardini et al.*, 2007]. The same method is applied for the upper interface z_s with a lower limit $z_s \ge z_b$.

Table 2. Durations and Fluidity Applied at Each Step of the Simulation HYST[a]

Name	Duration (ka)	B ($\mathrm{Pa}^{-3}\ \mathrm{a}^{-1}$)	T (deg C)
HYST step 1	30	$B_1 = 1.893 \times 10^{-17}$	−15
HYST step 2	15	$B_2 = 5/6 \times B1$	−17
HYST step 3	15	$B_3 = 2/3 \times B1$	−19
HYST step 4	15	$B_4 = 1/2 \times B1$	−21
HYST step 5	15	$B_5 = 1/3 \times B1$	−25
HYST step 6	30	$B_6 = 1/6 \times B1$	−30
HYST step 7	30	$B_7 = 1/12 \times B1$	−36
HYST step 8	15	$B_6 = 1/6 \times B1$	−30
HYST step 9	15	$B_5 = 1/3 \times B1$	−25
HYST step 10	30	$B_4 = 1/2 \times B1$	−21
HYST step 11	30	$B_3 = 2/3 \times B1$	−19
HYST step 12	30	$B_2 = 5/6 \times B1$	−17
HYST step 13	15	B_1	−15

[a]Values correspond to fluidities proposed in the MISMIP benchmark but expressed differently as here the fluidity parameter is $B = 2A$. However, numerically, the constitutive relations are rigorously the same. The last column gives an estimation of the corresponding ice temperature on the basis of interpolation data by *Paterson* [1994, chapter 5].

3.6. Mesh Refinement Around x_G

[33] As mentioned in the introduction, *Vieli and Payne* [2005] have highlighted the sensitivity of marine ice sheet models to their horizontal grid size. The method developed here does not derogate from this assertion as shown by sensitivity experiments presented by *Durand et al.* [2008]. Using a structured mesh composed of rectangular elements does not allow to access fine uniform grid resolution because of the induced numerical cost that rapidly becomes unmanageable. As fine grid resolution is only needed in the vicinity of the grounding line, a procedure that refines the mesh around the grounding line has been developed by *Durand et al.* [2008]. A constant grid size Δx_0 is set on an interval length L_f centered around x_G. Upstream of $x_G - L_f/2$ and downstream of $x_G + L_f/2$, a geometric progression of the horizontal extension of the elements is prescribed. The total number of elements on the horizontal direction is adjusted

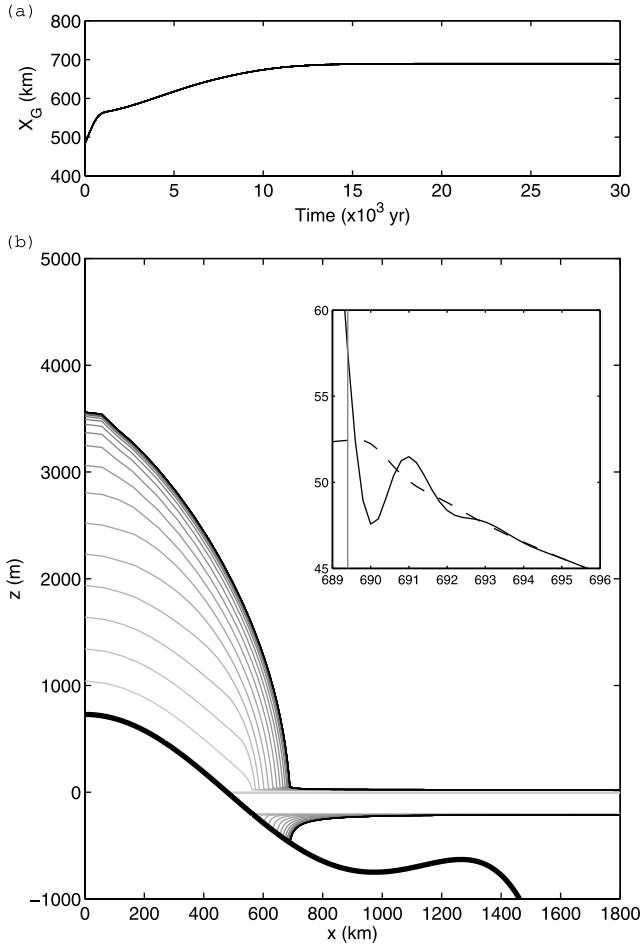

Figure 2. (a) Evolution of x_G over time for the first step of simulation HYST. (b) Surface profiles plotted every 1000 years. The steady state surface is plotted in black. The inset shows an enlargement of the upper surface (solid line) and is compared to the profile obtained for the floating surface (dashed line), whereas the vertical gray line marks the position of x_G.

so as to get reasonable progressions (i.e., <10% increase from one element to the next). Readjustment of the mesh is repeated after each displacement of the grounding line. Note that with this method the total number of nodes is constant and only the horizontal repartition of the nodes is modified. Simulations with a constant grid size set to Δx_0 everywhere give very similar results as simulations with the mesh refinement. In addition to the mesh refinement around x_G, some triangular elements can be introduced in order to merge two consecutive rows of elements. This significantly reduces the number of elements, saves computing resources and allows further investigation of marine ice sheet dynamics with very fine grid resolution (down to 30 m).

4. Simulations, Results, and Discussion

4.1. Settings of the Simulation

[34] The main aim of this paper is to confirm the hysteretic behavior of marine ice sheets as expected by the BL theory developed by *Schoof* [2007a]. As a consequence, numerical experiments have been performed using some of the settings presented by *Schoof* [2007b]. Particularly, we use the overdeepening bed defined by Schoof which, expressed in our reference frame, is given by

$$b(x) = 720 - 2184.8 \times \left(\frac{x}{750 \times 10^3}\right)^2 + 1031.72 \times \left(\frac{x}{750 \times 10^3}\right)^4 - 151.72 \times \left(\frac{x}{750 \times 10^3}\right)^6, \quad (16)$$

where x and b are in meters. The values of the physical constants used in this study are given in Table 1. Note that we used a constant accumulation rate $a_s = 0.3$ m a^{-1} over the whole domain, whereas accretion melting is neglected below the ice shelf. In this first set of simulations, the ice body is discretized with rectangular elements, $N_{bx} = 300$ elements in the horizontal direction and $N_{by} = 30$ equal thickness layers in the vertical direction (i.e., for a given x, nodes are evenly distributed on the vertical between bed or sea and ice/air interface).

[35] In order to highlight the hysteretic behavior of marine ice sheets, we followed *Schoof* [2007b]: during the simulation hereafter denoted HYST, the ice sheet is successively subjected to step changes of the fluidity following values proposed in MISMIP (Schoof et al., 2008; available at http://homepages.ulb.ac.be/∼fpattyn/mismip/) (see values in Table 2). The geometry of the ice sheet is initiated to a 10-m layer of ice on land extending up to the position where this layer becomes afloat ($x_G = 482.4$ km for the prescribed ρ_i and ρ_w (see Table 1)). Downstream of x_G and up to the end of the domain ($x = 1800$ km), an initial 10-m thick ice

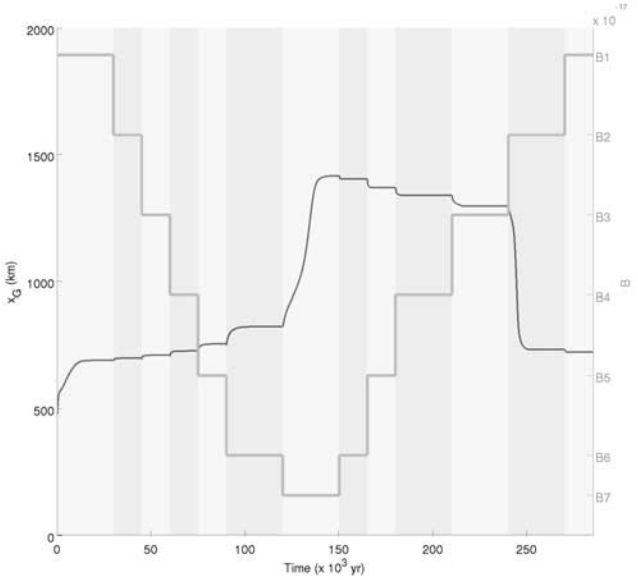

Figure 3. Evolutions of the grounding line (black line, left axis) and the prescribed fluidity (thick gray line, right axis) through time for the whole simulation HYST.

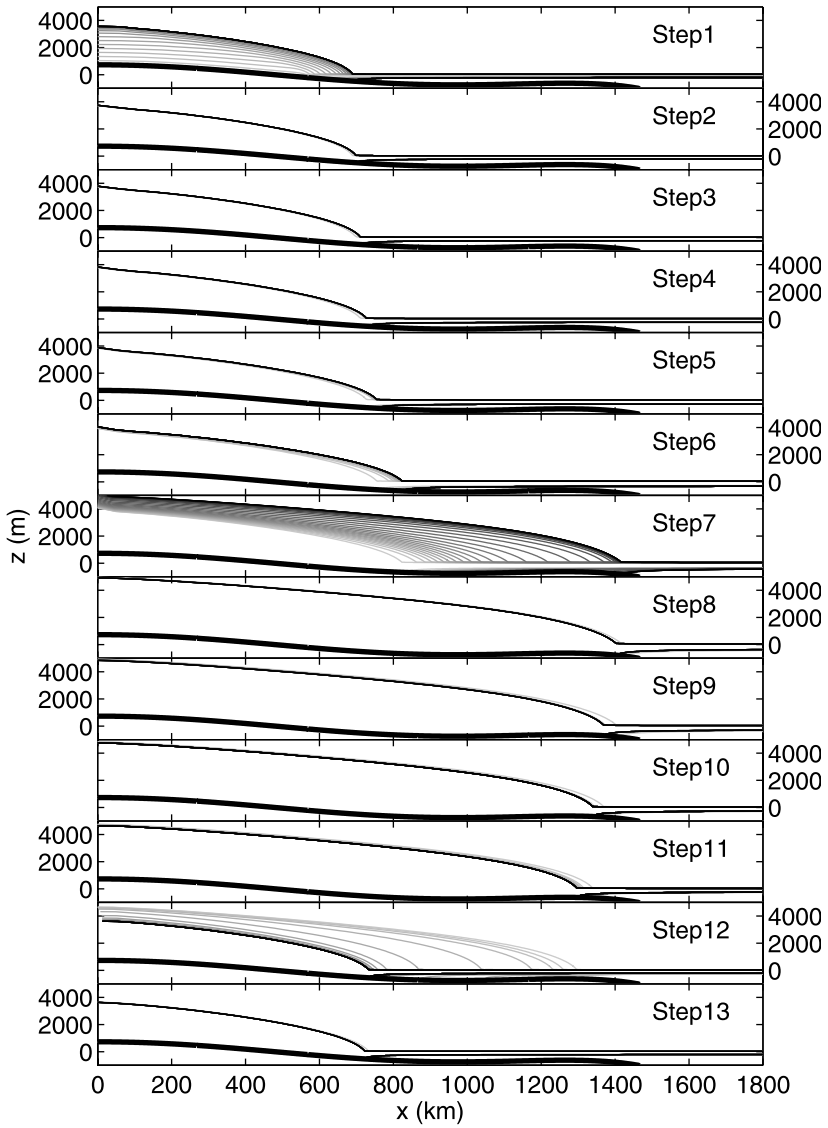

Figure 4. Surface profiles obtained every 1000 years in gray level for step 1 to step 13 of simulation HYST. The steady state profile for each step is plotted with a black line. Duration and prescribed fluidity for each step are defined in Table 2.

shelf extends the grounded part. Time spans of the different steps of the simulation are presented in Table 2. Note that a steady state (defined as a relative variation of volume smaller than 1×10^{-6}) is reached after each forcing step.

4.2. Steady State Air/Ice Surface

[36] As already mentioned, the first step of the simulation is launched starting from a 10-m layer of ice with an applied fluidity B_1 (see Table 2). Evolution of x_G is plotted over time in Figure 2a and surface profiles every 1000 years are presented in Figure 2b. First, because of the accumulation over the shelf and weak fluxes at the grounding line as well as at the calving front, the ice shelf rapidly thickens (232.1 m at t = 1500 years) and almost reaches its steady thickness (234.5 m). This thickening comes with a sinking of the ice shelf, which explains the rapid advance of x_G observed during the first 1500 years. Then, the shelf is close to equilibrium (entering flux almost equals the flux at the calving front) and the grounded ice sheet grows with a more limited impact on the advance of the grounding line. The steady state is finally reached after 18.5 ka for x_G = 689.4 km.

[37] Whereas most marine ice sheet models apply a flotation criterion at the sea/ice interface [*Huybrechts and de Wolde*, 1999; *Ritz et al.*, 2001], here the buoyancy stress exerted by the water is prescribed. Therefore, it is interesting to check if this applied stress condition leads to a floating ice shelf at the steady state. The upper steady state surface in the vicinity of the grounding line is plotted in the inset of Figure 2b. The surface corresponding to the flotation criterion deduced from the basal interface as $z_{fl} = z_b\,(\rho_w/\rho_i - 1)$ is plotted as well. The applied buoyancy condition leads to the development of a small depression downstream of x_G (approximatively 2 km long and 5 m deep), followed by slight surface oscillations. Note that such a depression appears immediately during the transient phase as it starts

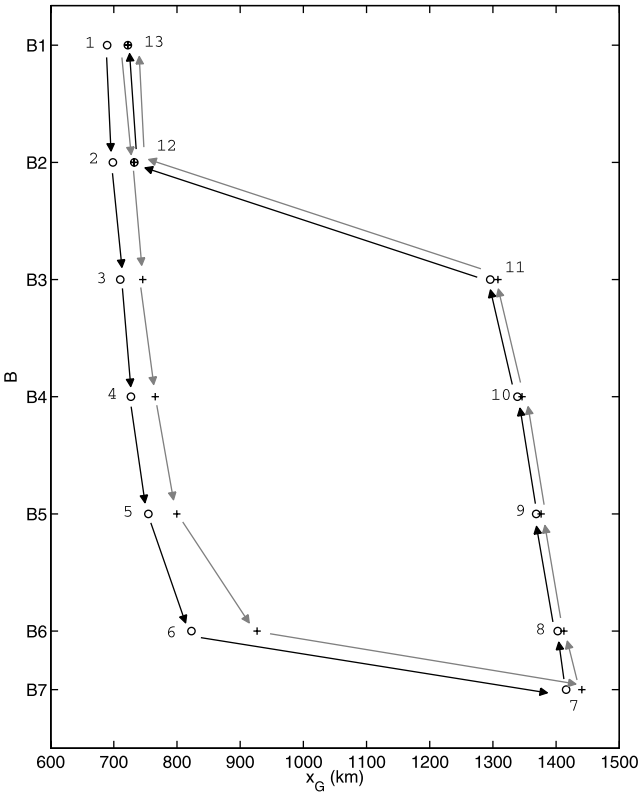

Figure 5. Evolution of the steady grounding line position versus the applied fluidity (open circles) for step 1 to step 13 of simulation HYST. Crosses depict results obtained by BL theory (Schoof, personal communication, 2008).

to form after the first time step. Such a pattern is classically observed at the upper surface lying above a drastic change in the basal condition, i.e., at the grounding line [*Anandakrishnan et al.*, 2007] or at transitions between the bedrock and a subglacial lake [*Bell et al.*, 2006, 2007]. This result is in full agreement with previous modeling work done by *Lestringant* [1994].

[38] As a consequence of these surface oscillations, the ice shelf does not comply with the flotation condition. However, this is a very local feature as the shelf is at flotation approximately 5 km downstream of x_G. Despite the very small area concerned, the application of a flotation criterion may affect the grounding line dynamics and then the evolution of modeled marine ice sheets. However, a new development of BL theory (Schoof, personal communication, 2009), which incorporates deviation from hydrostatic equilibrium, shows no change of grounding line steady state positions.

4.3. Hysteresis

[39] The simulation is pursued with prescribed step changes of the fluidity as presented in Table 2 and plotted in Figure 3. The evolution of the grounding line position through time can be seen in Figure 3 as well, whereas some of the obtained surface profiles are plotted in Figure 4. After a first steady state obtained during step 1, the evolution of the ice sheet is relatively slow until step 6 (x_G = 822.8 km). This rather limited advance relative to the important perturbation applied is explained by the large absolute value of the slope in this region. Indeed, once the grounding line reaches flat bedrock the rate of advance increases (step 6). Step 7 marks a drastic change in the dynamics of the grounding line as no steady state on the upsloping bed area can be found (between x = 973.7 and 1265.7 km). A new steady position of the grounding line is found once the overdeepening has been passed through for x_G = 1416.0 km.

[40] Such a drastic advance corresponds to a 120% increase of the total volume in 30 ka. Once the fluidity has reached its lowest value during step 7, it is reset step by step to its previous values (see Figure 3). Despite the fact that the fluidity prescribed during step 8 is equal to the fluidity applied during step 6 ($B = B_6$ (see Table 2)), steady states in both cases differ significantly. This is a clear illustration of the hysteretic behavior of marine ice sheets, as demonstrated by *Schoof* [2007a] using the BL theory. Increase of the fluidity from B_6 to B_3 induces a slight retreat of the grounding line, but x_G still lies on the continental slope. Fluidity needs to be reset to B_2 for the grounding line to be able to cross back through the overdeepening. As in the advancing phase, no steady state is found on the upsloping bed area. Further increase of the fluidity to its initial value B_1 leads to a limited retreat as the grounding line has reached again the strongly inclined downsloping bed area.

[41] The previous description of grounding line dynamics can be summarized by plotting the grounding line position reached at the steady state as a function of the prescribed fluidity (see Figure 5). Results obtained from BL theory with model B of *Schoof* [2007b] are presented as well. The upsloping bed region (between approximatively 970 and 1265 km), where no steady state can be found, clearly shows up. Results from the present work are qualitatively in good agreement with the ones obtained from the BL theory. Particularly, the passage across the upsloping bed area occurs for the same fluidity values (step 7 and 12). However, there is a shift between the two approaches, as BL theory predicts slightly more advanced grounding line positions. This is obvious for the first six steps, where a 104 km difference in x_G is found for step 6. It is however no longer the case from steps 8 to 13 where BL theory and the present approach give similar results. This is particularly striking for steps 12 and 13 where results differs by only 0.2%. All these steps correspond to positions obtained during the retreat of the grounding line. For a given fluidity, the retreating phase of the ice sheet leads to a different steady state position compared to the advancing phase (steps 12 and 13 (see Table 2 and Figure 5)). This indicates that marine ice sheet may show a neutral equilibrium within a given spatial range. Such a result would conflict with BL outcomes. However, the numerical method described here is known to be highly sensitive to grid resolution. Although its robustness has been demonstrated for advancing phase with horizontal mesh extension below 5 km [*Durand et al.*, 2008], this has to be further investigated during the retreating phase and is discussed in section 4.4.

4.4. Neutral Equilibrium: Still a Mesh Sensitivity Effect?

[42] A second experiment has been designed using results from simulations HYST in order to validate (or not) the neutral equilibrium hypothesis. Although all the simulation parameters are rigorously identical, HYST steps 2 and 12 present significantly different steady x_G (698.4 and 732.4 km,

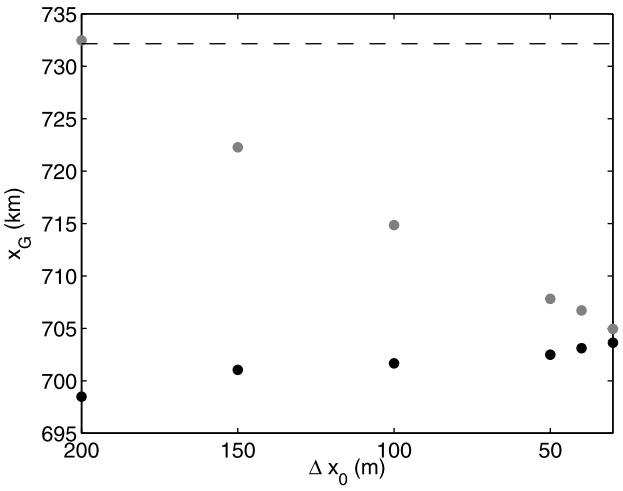

Figure 6. Evolution of the steady grounding line position as a function of the horizontal mesh extension Δx_0. Black circles (gray circles) represent results obtained for simulations starting from the steady state obtained after HYST step 2 (HYST step 12). Dashed line depicts results obtained by BL theory (Schoof, personal communication, 2008).

respectively). We now investigate whether these steady profiles are sensitive to mesh resolution. For that purpose, the corresponding steady state geometries have been remeshed using finer grids with Δx_0 = 200, 150, 100, 50, 40, 30 m and L_f = 2 km and the geometry was evolved to a new steady state. As mentioned in section 3.6 some triangular elements have been introduced upstream and downstream of the refined area in order to merge raws of elements and allow to compute new steady states in a reasonable time. Results are compiled in Figure 6 where steady x_G are plotted as a function of Δx_0. We were not able to obtain proper steady states with $\Delta x_0 < 50$ m as the volume was respecting the previously defined criterium (relative variation lower than 1×10^{-6}, see section 4.1) but x_G was continuously fluctuating between 2 nodes.

[43] Figure 6 shows that the spatial range where the modeled ice sheet presents a neutral equilibrium rapidly decreases from 34 km to less than 2 km with increasing resolution (Δx_0 = 200 and 30 m, respectively). We were unfortunately unable to fully remove neutral equilibrium behavior of our modeling approach and a residual neutral equilibrium about 2 km wide persists with the finest mesh we used. However, the grid refinement exercise indicates that the neutral equilibrium observed in experiment HYST is essentially a numerical artefact. This would confirm recent results from BL theory and full Stokes modeling approach by *Nowicki and Wingham* [2008]: a marine ice sheet sliding over its bed presents well defined discrete equilibrium profiles (if they have any at all, see section 4.3).

[44] From this last experiment, it clearly appears that mesh resolution around the grounding line is a crucial issue to properly model marine ice sheet dynamics with a full Stokes finite element approach: the use of too coarse a grid strongly affects the dynamics of the whole ice sheet. Indeed, the resolution of 200 m used in the HYST simulation proved too coarse, even though it was already quite small in comparison with the horizontal extent of the ice sheet. Our results indicate that the resolution has to be increased to tens of meters to yield consistent results. This will be particularly restrictive for future development as moving such a fine resolution to 3-D geometries would have an enormous computational cost. Efforts will have to be done to find the optimal mesh that allows a proper modeling and using higher-order elements is probably the first direction of investigation to follow.

5. Conclusions

[45] Motivated by the importance of marine ice sheets in the climatic system and a three decades long debate dealing with their stability, we modeled the grounding line dynamics using the FE code Elmer. The full Stokes velocity field along a flow line is computed and coupled with the air ice–free as well with as the sea ice–free interfaces. The grounding line is treated dynamically during the Stokes solution process and its position is determined by solving the contact problem between the ice and rigid bedrock. The problem is highly nonlinear as the implemented flow and friction laws are nonlinear and the position of the grounding line can change during the evolution (thus affecting the boundary condition).

[46] We used the modeling framework defined by *Schoof* [2007b] to study marine ice sheet behavior. The application of the water pressure on the ice/sea interface induces the formation of small depressions of the upper surface in the vicinity of the grounding line. As a consequence of these oscillations, the common assumption of local hydrostatic equilibrium is violated from x_G to approximatively 5 km downstream. This confirms previous modeling work from *Lestringant* [1994].

[47] In agreement with the BL theory results [*Schoof*, 2007a], a marine ice sheet is unstable on an upsloping bed, confirming once again the marine ice sheet instability hypothesis proposed by *Weertman* [1974]. Results are qualitatively in good agreement with BL theory predictions, particularly, the passage through the upsloping bed area occurs for the same fluidity values. Despite important numerical issues related to mesh resolution in the vicinity of the grounding line, our study confirms semianalytical results from *Schoof* [2007b] and numerical modeling from *Nowicki and Wingham* [2008]: 2-D marine ice sheet sliding over a downsloping bed presents a finite number of steady states; that is, it does not exhibit a neutral equilibrium.

[48] The mesh resolution is a crucial issue for a proper modeling of the dynamics of marine ice sheets. Indeed, too coarse a grid around the grounding lines prevents the ice sheet from retreating. This affects the dynamics of the whole ice sheet as this induces no physical neutral equilibrium. This may be solved by implementing a very small grid, even if, despite our effort, a residual neutral equilibrium about 2 km wide remains with the finest mesh we used (30 m). Such a result has important consequences in term of future development. Requirement in terms of mesh resolution will induce huge computing resources when dealing with a more physical 3-D geometry. Optimization of the mesh, in terms of spatial repartition as well as the type of elements used, will be a crucial issue.

Notation

a_s surface accumulation (m a^{-1})
b bedrock elevation (m)

B fluidity parameter ($Pa^{-3}\ a^{-1}$)
C sliding parameter ($Pa\ m^{-1/3}\ a^{1/3}$)
C_n buoyancy sliding parameter ($Pa\ m^{-1}\ a$)
$\mathbf{D}$ strain rate tensor (a^{-1})
$\mathbf{g}$ gravitational acceleration ($m\ s^{-2}$)
n power law exponent
m friction law exponent
$\mathbf{n}$ normal outward unit vector
p pressure (Pa) (Compressive positive)
p_w water pressure (Pa)
$\mathbf{S}$ deviatoric stress tensor (Pa)
$\mathbf{t}$ tangential vector
$\mathbf{u}$ velocity vector ($m\ a^{-1}$)
$\mathbf{x}$ coordinate vector (m)
x_G grounding line abscissa (m)
γ_e second invariant of the strain rate (a^{-1})
η effective viscosity (Pa a)
$\boldsymbol{\sigma}$ Cauchy stress tensor (Pa)
τ_b basal drag (Pa)
ρ_i ice density ($kg\ m^{-3}$)
ρ_w water density ($kg\ m^{-3}$)
z_s elevation of upper interface (m)
z_b elevation of bottom interface (m)
z_{fl} elevation of hydrostatic equilibrium surface (m)

[49] **Acknowledgments.** This research is part of the DACOTA project (ANR-06-VULN-016-01) funded by the Agence National de la Recherche. Most of the computations presented in this paper were performed at the Service Commun de Calcul Intensif de l'Observatoire de Grenoble. We are grateful to C. Schoof, R. Hindmarsh, and M. Lüthi for their very helpful comments. The authors would like to thank Peter Råback (CSC) for his support on the implementation of the time-dependent scheme for the buoyancy stress condition; Juha Ruokolainen (CSC) for his efficient assistance in numerical implementation; Mikko Lyly (CSC), who helped develop the contact scheme; and reviewers for their meaningful comments.

References

Alley, R., P. Clark, P. Huybrechts, and I. Joughin (2005), Ice-sheet and sea-level changes, *Science*, *310*, 456–460, doi:10.1126/science.1114613.

Anandakrishnan, S., G. Catania, R. Alley, and H. Horgan (2007), Discovery of till deposition at the grounding line of Whillans Ice Stream, *Science*, *315*, 1835–1838, doi:10.1126/science.1138393.

Baiocchi, C., F. Brezzi, and L. P. Franca (1993), Virtual bubbles and the Galerkin least squares method, *Comput. Methods Appl. Mech. Eng.*, *105*, 125–141.

Bell, R. E., M. Studinger, M. A. Fahnestock, and C. A. Shuman (2006), Tectonically controlled subglacial lakes on the flanks of the Gamburtsev Subglacial Mountains, East Antarctica, *Geophys. Res. Lett.*, *33*, L02504, doi:10.1029/2005GL025207.

Bell, R. E., M. Studinger, C. A. Shuman, M. A. Fahnestock, and I. Joughin (2007), Large subglacial lakes in East Antarctica at the onset of fast-flowing ice streams, *Nature*, *445*(7130), 904–907, doi:0.1038/nature05554.

Chugunov, V., and A. Wilchinsky (1996), Modelling of a marine glacier and ice-sheet ice-shelf transition zone based on asymptotic analysis, *Ann. Glaciol.*, *23*, 59–67.

Donea, J., and A. Huerta (2003), *Finite Element Methods for Flow Problems*, John Wiley, Chichester, U. K.

Durand, G., O. Gagliardini, T. Zwinger, and E. Le Meur (2008), Full-stokes modeling of marine ice-sheets: Influence of the grid size, *Ann. Glaciol.*, in press.

Gagliardini, O., and T. Zwinger (2008), The ISMIP-HOM benchmark experiments performed using the finite-element code Elmer, *Cryosphere Discuss.*, *2*(1), 75–109.

Gagliardini, O., D. Cohen, P. Råback, and T. Zwinger (2007), Finite-element modeling of subglacial cavities and related friction law, *J. Geophys. Res.*, *112*, F02027, doi:10.1029/2006JF000576.

Hindmarsh, R. (1993), Qualitative dynamics of marine ice sheets, in *Ice in the Climate System*, edited by W. R. Peltier, pp. 68–99, Springer, Berlin.

Hindmarsh, R. (1996), Stability of ice rises and uncoupled marine ice sheets, *Ann. Glaciol.*, *23*, 105–115.

Huybrechts, P. (1997), Report of the third EISMINT workshop on model intercomparison, technical report, EISMINT Intercomparison Group, Grindelwald, Switzerland.

Huybrechts, P., and J. de Wolde (1999), The dynamic response of the Greenland and Antarctic ice sheets to multiple-century climatic warming, *J. Clim.*, *12*(8), 2169–2188.

Huybrechts, P., T. Payne, A. Abe-Ouchi, and R. Calov (1996), The EISMINT benchmarks for testing ice-sheet models, *Ann. Glaciol.*, *23*, 1–12.

Iken, A. (1981), The effect of the subglacial water pressure on the sliding velocity of a glacier in an idealized numerical model, *J. Glaciol.*, *27*, 407–421.

Intergovernmental Panel on Climate Change (2007), *Climate Change 2007: The Physical Science Basis: Working Group I Contribution to the Fourth Assessment Report of the IPCC*, edited by S. Solomon et al., Cambridge Univ. Press, New York.

Lestringant, R. (1994), A two-dimensional finite-element study of flow in the transition zone between an ice sheet and an ice shelf, *Ann. Glaciol.*, *20*, 67–71.

Nowicki, S. M. J., and D. J. Wingham (2008), Conditions for a steady ice sheet–ice shelf junction, *Earth Planet. Sci. Lett.*, *265*(1–2), 246–255.

Paterson, W. S. B. (1994), *The Physics of Glaciers*, Pergamon, Oxford, U. K.

Pattyn, F., A. Huyghe, S. De Brabander, and B. De Smedt (2006), Role of transition zones in marine ice sheet dynamics, *J. Geophys. Res.*, *111*, F02004, doi:10.1029/2005JF000394.

Payne, A. J., A. Vieli, A. P. Shepherd, D. J. Wingham, and E. Rignot (2004), Recent dramatic thinning of largest West Antarctic ice stream triggered by oceans, *Geophys. Res. Lett.*, *31*, L23401, doi:10.1029/2004GL021284.

Rignot, E. J. (1998), Fast recession of a West Antarctic glacier, *Science*, *281*, 549–551, doi:10.1126/science.281.5376.549.

Rignot, E., D. G. Vaughan, M. Schmeltz, T. Dupont, and D. MacAyeal (2002), Acceleration of Pine Island and Thwaites Glaciers, West Antarctica, *Ann. Glaciol.*, *34*, 189–194, doi:10.3189/172756402781817950.

Ritz, C., V. Rommelaere, and C. Dumas (2001), Modeling the evolution of Antarctic ice sheet over the last 420,000 years: Implications for altitude changes in the Vostok region, *J. Geophys. Res.*, *106*, 31,943–31,964, doi:10.1029/2001JD900232.

Schoof, C. (2005), The effect of cavitation on glacier sliding, *Proc. R. Soc., Ser. A*, *461*(2055), 609–627, doi:10.1098/rspa.2004.1350.

Schoof, C. (2007a), Marine ice-sheet dynamics. Part 1. The case of rapid sliding, *J. Fluid Mech.*, *573*, 27–55, doi:10.1017/S0022112006003570.

Schoof, C. (2007b), Ice sheet grounding line dynamics: Steady states, stability, and hysteresis, *J. Geophys. Res.*, *112*, F03S28, doi:10.1029/2006JF000664.

Van der Veen, C. (1985), Response of a marine ice sheet to changes at the grounding line, *Quat. Res.*, *24*, 257–267.

Vieli, A., and A. J. Payne (2005), Assessing the ability of numerical ice sheet models to simulate grounding line migration, *J. Geophys. Res.*, *110*, F01003, doi:10.1029/2004JF000202.

Weertman, J. (1974), Stability of the junction of an ice sheet and an ice shelf, *J. Glaciol.*, *13*, 3–11.

B. de Fleurian, G. Durand, O. Gagliardini, and E. Le Meur, Laboratoire de Glaciologie et Géophysique de l'Environnement, UJF-Grenoble, CNRS, BP 96, F-38402 Saint-Martin-d'Hères, France. (fleurian@lgge.obs.ujf-grenoble.fr; durand@lgge.obs.ujf-grenoble.fr; gagliar@lgge.obs.ujf-grenoble.fr; lemeur@lgge.obs.ujf-grenoble.fr)

T. Zwinger, CSC-IT Center for Science Ltd., P.O. Box 405, FI-02101 Espoo, Finland. (zwinger@csc.fi)